



Title	High wavelength-resolution Bragg-edge/dip transmission imaging instrument with a supermirror guide-tube coupled to a decoupled thermal-neutron moderator at Hokkaido University Neutron Source
Author(s)	Sato, Hiroataka; Sasaki, Tsukasa; Moriya, Takahiro; Ishikawa, Hirotaku; Kamiyama, Takashi; Furusaka, Michihiro
Citation	Physica B : Condensed Matter, 551, 452-459 https://doi.org/10.1016/j.physb.2017.12.058
Issue Date	2018-12-15
Doc URL	http://hdl.handle.net/2115/79940
Rights	© <2018>. This manuscript version is made available under the CC-BY-NC-ND 4.0 license http://creativecommons.org/licenses/by-nc-nd/4.0/
Rights(URL)	http://creativecommons.org/licenses/by-nc-nd/4.0/
Type	article (author version)
File Information	ICNS2017_proc_sato_v7.pdf



[Instructions for use](#)

1 **High wavelength-resolution Bragg-edge/dip**
2 **transmission imaging instrument with a supermirror**
3 **guide-tube coupled to a decoupled thermal-neutron**
4 **moderator at Hokkaido University Neutron Source**

5
6 Hiroataka Sato*, Tsukasa Sasaki, Takahiro Moriya, Hirotaku Ishikawa, Takashi Kamiyama
7 and Michihiro Furusaka

8
9 Graduate School of Engineering, Hokkaido University, Kita-13 Nishi-8, Kita-ku, Sapporo
10 060-8628, Japan

11
12 *Corresponding author. Tel.: +81-11-706-6679; Fax: +81-11-706-6679.

13 E-mail address: h.sato@eng.hokudai.ac.jp

14
15 **ABSTRACT**

16 Bragg-edge neutron transmission imaging is one of several useful material
17 characterization tools available at a compact-accelerator driven pulsed-neutron source (a
18 pulsed CANS). Quantitative imaging experiments for crystalline phase, crystallographic
19 texture, and crystallite size have been successfully performed at a pulsed CANS using a
20 coupled (high intensity type) cold-neutron moderator. However, imaging experiments for
21 strain and grain orientation have not been achieved due to the low wavelength-resolution
22 of the coupled moderator. In this study, we demonstrated that both strain imaging using
23 the Bragg-edge transmission method and grain-orientation imaging using the Bragg-dip
24 transmission method are feasible at a pulsed CANS; both types of imaging are made
25 possible with an efficient neutron beam transport system using a supermirror guide-tube
26 combined with a decoupled thermal-neutron moderator (300 K polyethylene), which can
27 supply short neutron pulse. Using this system, we achieved high wavelength-resolution
28 (about 0.5%) Bragg-edge/dip neutron transmission imaging experiments, which correctly
29 visualized the strain values and grain orientations in several polycrystalline materials. On
30 the other hand, it was also found that the neutron flux and the neutron beam angular
31 divergence (L/D) were insufficient with this approach. For this reason, we performed
32 Monte-Carlo simulation studies to investigate a new geometry of moderator system which
33 achieves not only high wavelength-resolution (short pulse width) but also high neutron
34 brightness which is necessary for a high L/D experiment. The simulation results suggest
35 that the most promising candidates use a thin and low-height cold-neutron moderator (20

36 K methane) with decoupled pre-moderators or poisoned pre-moderators with large solid-
37 angle coverage for fast neutrons emitted from a neutron production target. This system
38 offers higher peak intensity than a coupled moderator for cold neutrons emitted from the
39 highest brightness region on the moderator surface, while achieving narrow pulse widths
40 and decay times as fast as those of decoupled/poisoned moderators.

41
42 **Keywords:** Compact-accelerator driven pulsed-neutron source; Decoupled moderator;
43 Supermirror guide-tube; Bragg-edge/dip; Strain imaging; Grain orientation imaging
44

45 **1. Introduction**

46 A compact-accelerator driven pulsed-neutron source (i.e., a pulsed CANS) is expected
47 to offer several useful tools for crystallographic and metallurgical research [1]. Among
48 the most promising tools are Bragg-edge [2-5] and Bragg-dip [6] neutron transmission
49 imaging methods using the time-of-flight (TOF) spectroscopy. This is because
50 visualization of crystallographic information can be easily performed with a neutron
51 transmission geometry using a single neutron TOF-imaging detector. Using these
52 methods, non-destructive testing of crystalline materials have been successfully
53 performed at the Hokkaido University Neutron Source (HUNS) [7] which is a pulsed
54 CANS with a yield on the order of 10^{12} neutrons/sec. These tests yielded quantitative
55 visualizations of crystalline phase [8], crystallographic texture [2], and crystallite size [2]
56 in a thick metallic material. In particular, we have carried out these tests using a coupled
57 cold-neutron moderator because Bragg-edges around the cold-neutron energy region are
58 frequently analyzed. Furthermore, we exported some of these techniques to J-PARC MLF
59 BL22 “RADEN” [9] which is the first energy-resolved neutron imaging instrument
60 constructed at a world-leading pulsed spallation neutron source facility.

61 A coupled moderator [10] is suitable for a pulsed CANS because it can supply a higher
62 intensity of neutrons than a decoupled moderator and a decoupled-poisoned moderator.
63 However, a coupled moderator provides lower TOF (wavelength) resolution beams due
64 to its broad neutron pulse. Since high wavelength-resolution is required for both lattice-
65 strain imaging using the Bragg-edge method [4,5] and crystalline grain-orientation
66 imaging using the Bragg-dip method [6], neither of these measurements have been
67 achieved with 10 m-class beam-lines in a pulsed CANS using a coupled moderator. This
68 is because the wavelength resolution of the coupled moderator and short beam-line setup
69 is several percent. For successful use of these imaging techniques to measure sharp
70 Bragg-edge/dip, and to analyze the clear edge/dip profile, a wavelength resolution of
71 around 0.5% is necessary. Therefore, in a previous work [1], we proposed to use both a

72 decoupled moderator for higher wavelength-resolution and a supermirror guide-tube for
73 recovering the neutron flux decreased by the decoupled moderator, as suggested by
74 Monte-Carlo simulation studies.

75 In this study, we experimentally demonstrated strain and grain-orientation imaging
76 using a supermirror guide-tube coupled to a decoupled moderator at ambient temperature
77 at HUNS. This moderator condition (decoupled thermal-neutron moderator) decreases
78 the neutron flux to the minimum level for CANS, although the wavelength resolution is
79 drastically improved. For this reason, we also investigated better cold-neutron moderator
80 systems in this study, using Monte-Carlo simulations of neutron transport. Finally, in this
81 paper, we report the possibility of two novel types of moderator systems, a cold-neutron
82 moderator with a decoupled pre-moderator and a poisoned pre-moderator.

84 **2. Strain and grain-orientation imaging at a compact-accelerator driven** 85 **pulsed-neutron source**

86 In this section, we report the first strain and grain-orientation imaging results obtained
87 at a pulsed CANS. The experimental setup and the neutron beam performances are also
88 presented.

90 **2.1. Specimens**

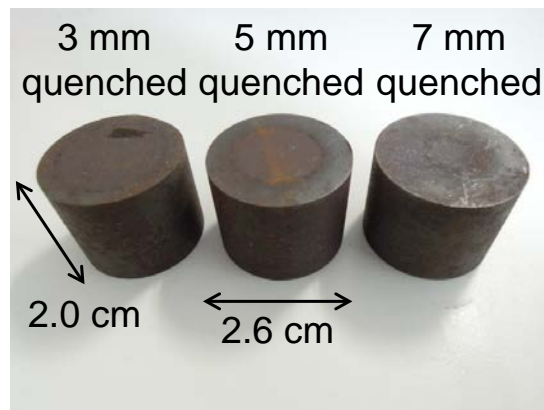
91 Fig. 1 shows three samples to demonstrate strain imaging using the Bragg-edge method.
92 The steel type was JIS-SCM440, using the Japanese Industrial Standards designation, and
93 the dimensions were 26 mm in diameter and 20 mm in height. The difference between
94 samples was the quenched depth from the outer rim. Each quenched depth given by the
95 induction hardening was 3 mm, 5 mm and 7 mm, respectively. As a result, ferrite
96 phase/microstructure remained in the center region, and martensite phase/microstructure
97 appeared near the rim. In the martensite region, fine microstructures were formed from a
98 solid solution of carbon atoms. Macro-strain is evaluated from the Bragg-edge shift, i.e.,
99 the change of average value of distribution of crystal lattice plane spacing (d -spacing).
100 Micro-strain is evaluated from the Bragg-edge broadening, i.e., the change of FWHM of
101 the d -spacing distribution. Both types of strain in the martensite region are larger than
102 those in the ferrite region. The strain imaging results from samples quite similar to these
103 have been obtained at J-PARC MLF BL10 “NOBORU” [11], and have been
104 quantitatively evaluated in a previous work [4]. In the present study, we compared new
105 results obtained at HUNS with the prior data from J-PARC.

106 Fig. 2 shows a sample to demonstrate grain-orientation imaging using the Bragg-dip
107 method. The grain-orientation image of this sample has been obtained at J-PARC MLF

108 BL10 “NOBORU” [11], and has been quantitatively evaluated in a previous work [6].
109 This sample was 6.9 cm × 6.1 cm × 5 mm thickness; it consisted of 3.4wt%Si steel, and
110 included large grains (nearly a centimeter in size). For the SEM-EBSD observations in
111 the previous work [6], the sample was separated into 9 pieces (see Fig. 2). We compared
112 the evaluated grain-orientation results between HUNS (this study) and J-PARC (previous
113 study) by using this sample.

114 In the experiment, these four samples were simultaneously measured owing to a large-
115 area (10 cm × 10 cm) neutron TOF-imaging detector as described below. The
116 measurement time for the open beam was 31 hours, and the measurement time for the
117 sample beam was 42 hours.

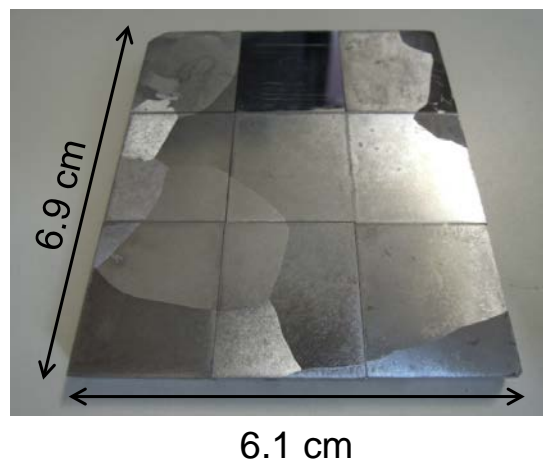
118



119

120 Fig. 1. Quenched ferritic steel rods for demonstration of strain imaging using the Bragg-
121 edge transmission method performed with high wavelength-resolution setup at HUNS.
122 The previous work performed at J-PARC was reported in Ref. [4].

123



124

125 Fig. 2. Si-steel plate with large crystalline grains for demonstration of grain-orientation

126 imaging using the Bragg-dip transmission method performed with high wavelength-
127 resolution setup at HUNS. The previous work performed at J-PARC was reported in Ref.
128 [6]. The sample was divided into 9 pieces for the SEM-EBSD observations after the
129 previous Bragg-dip neutron transmission imaging experiment.

130 131 **2.2. Experimental setup using a decoupled thermal-neutron moderator and a** 132 **supermirror guide-tube**

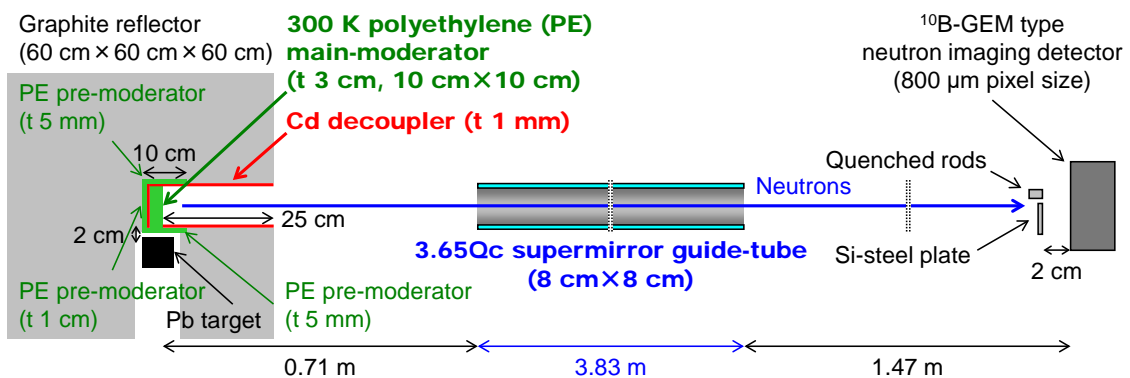
133 Fig. 3 shows a schematic layout of the experimental setup. HUNS is a pulsed neutron
134 source driven by an electron linear-accelerator at Hokkaido University (Hokkaido
135 LINAC). The electron beam power was 1.26 kW ($34 \text{ MeV} \times 37 \mu\text{A}$), the electron beam
136 pulse width was $3.4 \mu\text{s}$, and the pulse repetition rate was 50 Hz. Fast neutrons were
137 produced from a lead target ($7 \text{ cm} \times 7 \text{ cm} \times 7 \text{ cm}$) by photonuclear reaction after electron
138 bremsstrahlung.

139 In this experiment, the fast neutrons were converted to thermal neutrons by
140 polyethylene moderators at ambient temperature. Neutron beam extraction employed a
141 “wing” geometry. A graphite reflector and polyethylene pre-moderators were placed
142 around the polyethylene main-moderator. The reflector and the pre-moderators were
143 separated from the main-moderator by cadmium decouplers of 1 mm thickness, in terms
144 of thermal/cold neutrons. This geometry is similar to that of a poisoned pre-moderator
145 system (described below), but it is not effective for an ambient-temperature main-
146 moderator used with ambient-temperature pre-moderators. In any case, this decoupler
147 was a key component to achieve high wavelength-resolution (i.e., a narrow neutron pulse).
148 In addition, we adopted a thin main-moderator (3 cm thickness) as the other key
149 modification for high wavelength-resolution, although the surface area of the main-
150 moderator was the same as that of a traditional design ($10 \text{ cm} \times 10 \text{ cm}$). The thicknesses
151 of the pre-moderators were 1 cm (backside of the main-moderator) and 5 mm (mounted
152 on the side of the main-moderator).

153 For recovering low fluxes of cold neutrons due to the decoupled thermal-neutron
154 moderator, we mounted a supermirror guide-tube at a position 0.71 m from the moderator
155 surface. The supermirror guide-tube was 3.83 m in length, $8 \text{ cm} \times 8 \text{ cm}$ in area, and had
156 a 3.65Qc supermirror coating. The samples were positioned 1.45 m from the outlet of the
157 guide tube, and the neutron TOF-imaging detector was set 0.02 m from the samples. The
158 total neutron flight path length was 6.01 m. Note that these parameters were not optimized
159 because facility geometries, guide-tube length, radiation shields, and the sample-handling
160 space were all constrained.

161 The neutron TOF-imaging detector used in this experiment was a ^{10}B -GEM (gas

162 electron multiplier) type detector developed by Prof. S. Uno of KEK (High Energy
 163 Accelerator Research Organization) in Japan [12]. The detection area was $10.24 \text{ cm} \times$
 164 10.24 cm , and the pixel size was $800 \mu\text{m} \times 800 \mu\text{m}$. The TOF bin width was set at $10 \mu\text{s}$.
 165 The counting rate for the open beam during this experiment was relatively low, about
 166 $7.0 \times 10^2 \text{ events/cm}^2/\text{s}$, due to the limits of not only the detection efficiency (about 10%
 167 for cold neutrons) but also the low neutron flux. However, this counting rate approached
 168 that of our recent J-PARC experiment using the GEM detector, about 1.6×10^3
 169 $\text{events/cm}^2/\text{s}$ [6], which was the maximum achievable counting rate of the detector.
 170

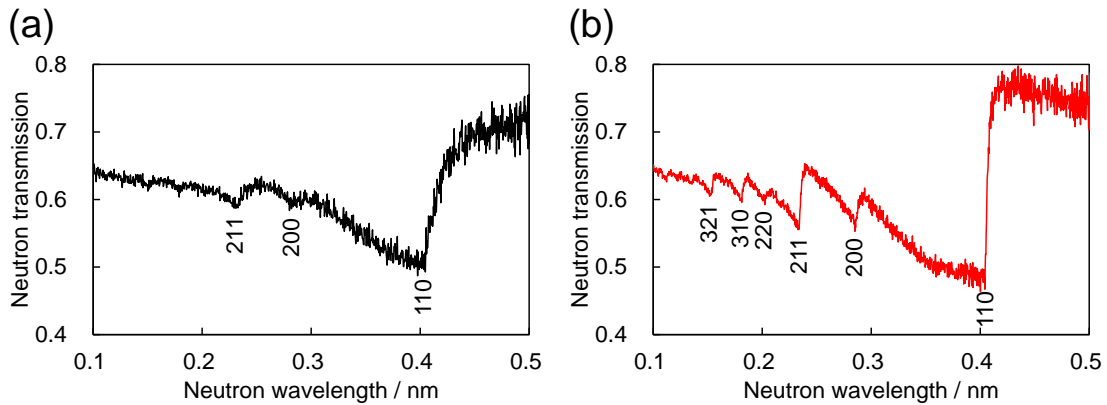


171
 172 Fig. 3. Schematic layout of the high wavelength-resolution Bragg-edge/dip transmission
 173 imaging instrument using a supermirror guide-tube coupled to a decoupled thermal-
 174 neutron moderator at HUNS.

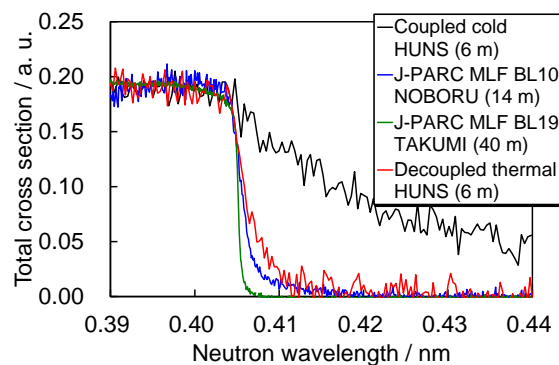
175
 176 **2.3. Neutron beam performance**

177 Fig. 4 shows the Bragg-edge neutron transmission spectra of α -Fe obtained using a
 178 coupled cold-neutron moderator (20 K mesitylene) and the present experimental setup, at
 179 HUNS. Fig. 5 shows the {110} Bragg-edge (normalized total cross-section expression)
 180 of α -Fe obtained using the facilities listed. By using these data, we discuss the wavelength
 181 resolution of the “decoupled thermal HUNS”. The Bragg-edge profile obtained using the
 182 decoupled thermal HUNS is sharper than that obtained using the coupled cold HUNS.
 183 The FWHM of the cold neutron pulse (wavelength 0.4 nm) emitted from the decoupled
 184 thermal HUNS was $35 \mu\text{s}$, and the achievable wavelength resolution at the 6 m position
 185 was 0.5%. This value was drastically improved over that obtained with the coupled cold
 186 HUNS (about 3% at 6 m) [2]. In addition, one of the features of the decoupled thermal
 187 HUNS was fast decay time, allowing better analysis of the Bragg-edge profile.
 188 Incidentally, this wavelength resolution approximates that of the J-PARC MLF
 189 instruments: the wavelength resolution at 14 m on BL10 “NOBORU” [11] which is

190 connected to a decoupled moderator (cold neutron pulse FWHM of 50 μs) is 0.35%, and
 191 the wavelength resolution at 40 m on BL19 “TAKUMI” [13] which is connected to a
 192 decoupled-poisoned moderator (cold neutron pulse FWHM of 30 μs) is 0.15%.
 193



194
 195 Fig. 4. Bragg-edge neutron transmission spectra of the same sample of $\alpha\text{-Fe}$, measured
 196 by (a) a coupled cold-neutron moderator and (b) a decoupled thermal-neutron moderator,
 197 at HUNS.
 198



199
 200 Fig. 5. Comparison of $\{110\}$ Bragg-edge profiles of $\alpha\text{-Fe}$ measured at various facilities.
 201

202 On the other hand, it was estimated that the cold neutron flux decreased due to the
 203 decoupled thermal-neutron moderator. According to Monte-Carlo simulation calculations,
 204 the cold neutron intensity of the decoupled 300 K polyethylene moderator is 1/30 of that
 205 of the coupled 20 K mesitylene moderator (i.e., a threefold reduction due to the decoupler
 206 and a tenfold reduction due to the polyethylene thermal-neutron moderator). However,
 207 owing to the supermirror guide-tube, the neutron transport efficiency was 10 times higher.
 208 As a result, the cold neutron flux of this experiment was estimated to be 1/3 of that of the
 209 coupled 20 K mesitylene HUNS without a guide tube. For future tests, a decoupled cold-
 210 neutron moderator should provide higher intensity neutron beams with better wavelength-

211 resolution than the traditional coupled moderator used with HUNS, owing to the
212 supermirror guide-tube configuration. The moderator should employ 20 K methane,
213 rather than 20 K mesitylene, since the former cold-neutron moderator provides the highest
214 intensity for a pulsed CANS system.

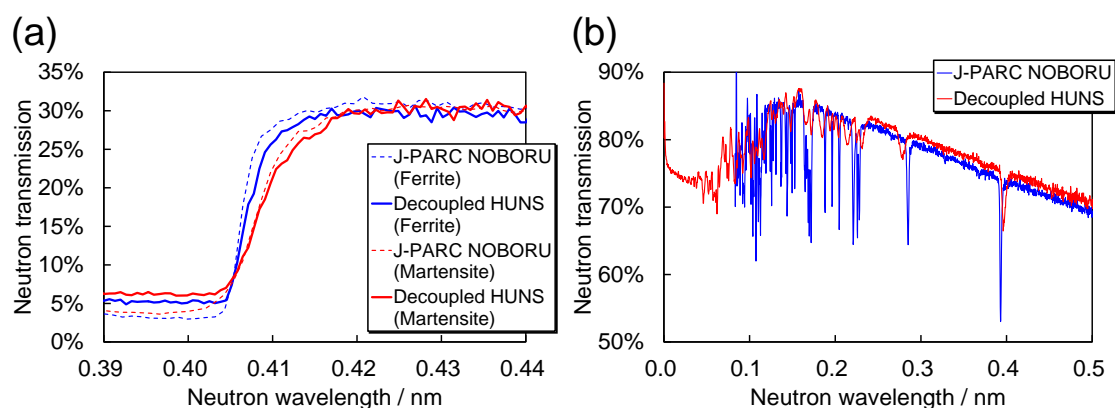
215

216 **2.4. Measured Bragg-edge/dip profiles**

217 Fig. 6 (a) shows a comparison of ferrite/martensite Bragg-edge transmission spectra
218 obtained by this experiment (HUNS) and the previous work (J-PARC) [4]. The spectra
219 slightly differ due to microstructure effects because different but similar samples were
220 measured. Qualitatively, the change in Bragg-edge broadening observed between ferrite
221 and martensite phases appeared to be the same at both facilities. A quantitative
222 comparison is discussed later by using strain imaging results.

223 Fig. 6 (b) shows a comparison of Bragg-dip transmission spectra obtained from coarse
224 grain (single crystal) samples as part of this experiment (HUNS) and in the previous work
225 (J-PARC) [6]. In the HUNS case, the Bragg-dip depth is not deep, and Bragg-dip width
226 is broad. This is due to both low wavelength-resolution (about 0.5% in the present
227 experiment, while that of the J-PARC experiment was about 0.35%) and low beam
228 angular divergence (the L/D ratio of this experiment was less than 60, but that of the J-
229 PARC experiment was about 2400 [6]). Thus, it was found that the Bragg-dip analysis is
230 easily affected by wavelength and angular resolutions in contrast to the Bragg-edge
231 analysis. As a result, grain-orientation imaging was relatively difficult, as discussed below.
232 Incidentally, the difference of Bragg-dip positions between this experiment and the
233 previous work was caused by differences in sample alignment between the neutron beam
234 direction and the normal direction of the sample plate. However, this effect is small for
235 the grain-orientation imaging result (see Fig. 9).

236



237

238 Fig. 6. Comparison of (a) Bragg-edge profiles and (b) Bragg-dip profiles between the

239 decoupled thermal HUNS and J-PARC MLF BL10 “NOBORU”. The spectra were
240 integrated over about 100 pixels in order to obtain better statistical data.

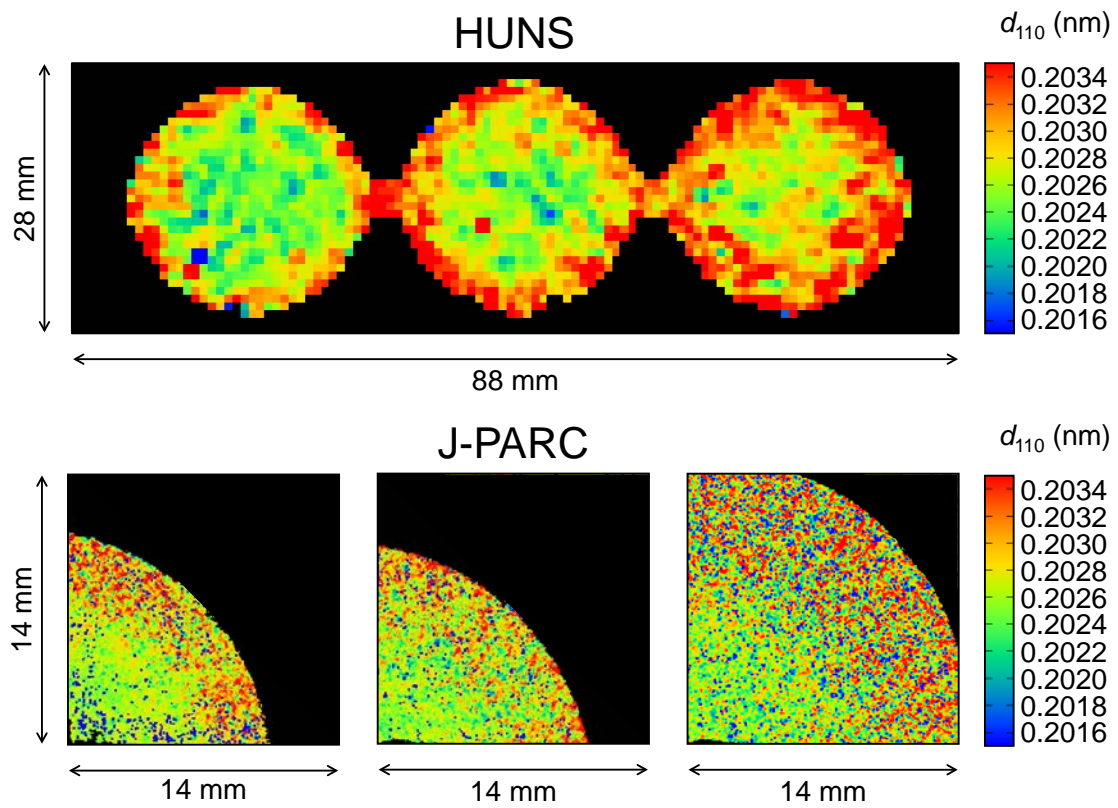
241

242 **2.5. Quantitative imaging results**

243 Figs. 7 and 8 show quantitative imaging results of average of d -spacing distribution,
244 d_{110} , relating to macro-strain (Fig. 7), and the FWHM of the d -spacing distribution, w_{110} ,
245 relating to micro-strain (Fig. 8) for ferrite/martensite rods, obtained by this experiment
246 (HUNS) and the previous work (J-PARC) [4]. Data from the present study were analyzed
247 in the same way as that of the previous work [4]. Both Figs. 7 and 8 show the samples
248 with quenched depths of 3 mm, 5 mm and 7 mm from left to right. Images in the upper
249 half of each figure are HUNS results, those of the lower half are J-PARC results. Note
250 that the pixel size of the imaging detector, the beam angular divergence, the accelerator
251 power and the measurement time all differed between these experiments. In the J-PARC
252 experiment, the pixel size was 55 μm owing to the MCP detector [14], the L/D ratio was
253 337, the accelerator power was 120 kW, and the measurement times were 22 hours for all
254 samples and 7 hours for the open beam, respectively [4]. For this reason, the spatial
255 resolution of the imaging results obtained at each facility is quite different.

256 It is remarkable that the values of d_{110} and w_{110} evaluated at both facilities are
257 consistent. As shown in Fig. 7, quantitative imaging results at both HUNS and J-PARC
258 indicate that d_{110} in the ferrite (center) region was 0.2026 nm (light-green color), and
259 0.2032 nm (red color) in the martensite (rim) region. In Fig. 8, w_{110} in the ferrite region
260 is seen to be less than 0.001 nm (blue color), and 0.002 ~ 0.004 nm (green ~ red color) in
261 the martensite (rim) region, both of which were correctly visualized by both the HUNS
262 and the J-PARC experiments. In addition, in both the d_{110} and the w_{110} imaging, HUNS
263 was able to visualize the radial dependence of quenched depth for each rod (3 mm, 5 mm
264 and 7 mm). These results confirm that a pulsed CANS used with a decoupled moderator
265 is effective for quantitative strain imaging.

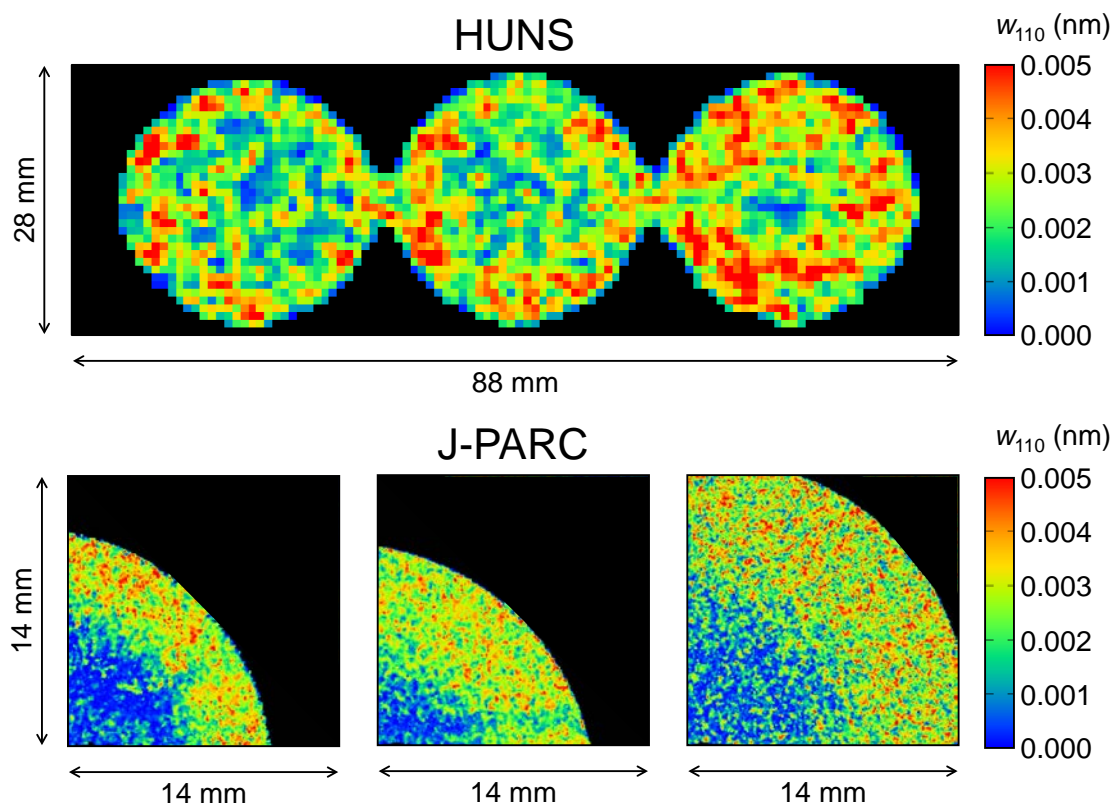
266



267

268 Fig. 7. Comparison of quantitative imaging results of average of d -spacing (crystal lattice
 269 plane spacing) distribution, relating to macro-strain, performed at HUNS and J-PARC.
 270 The J-PARC results were reported in Ref. [4].

271



272

273 Fig. 8. Comparison of quantitative imaging results of FWHM of d -spacing (crystal lattice
 274 plane spacing) distribution, relating to micro-strain, performed at HUNS and J-PARC.
 275 The J-PARC results were reported in Ref. [4].

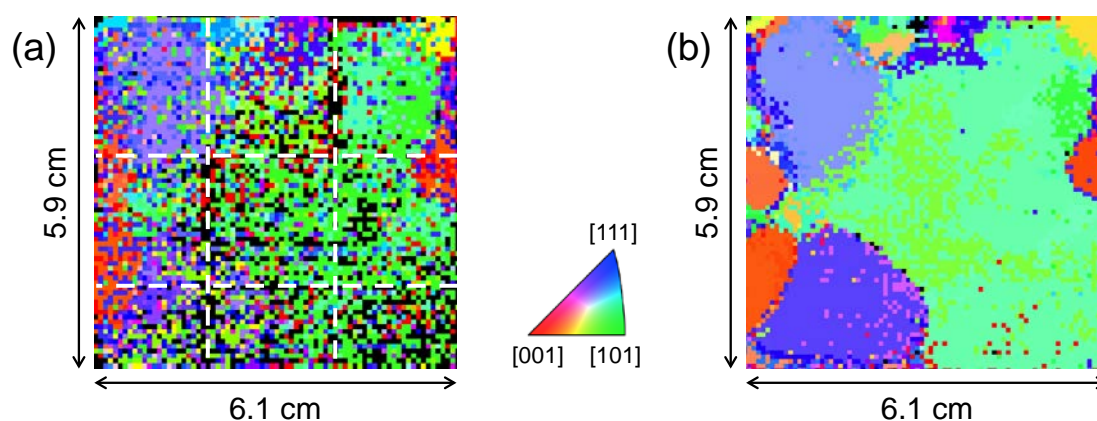
276

277 Fig. 9 shows the results of inverse pole figure (IPF) mapping to image grain orientation,
 278 using the Bragg-dip transmission method; the data shown were obtained by this
 279 experiment (HUNS) and the previous work (J-PARC) [6]. The grain-orientation image
 280 obtained at J-PARC was clearly visualized. Note that the beam angular divergence, the
 281 accelerator power and the measurement time were different between these experiments.
 282 In the J-PARC experiment, the L/D ratio was 2400, the accelerator power was 500 kW,
 283 and the measurement times were 14.5 hours for the sample beam and 7.2 hours for the
 284 open beam [6]. On the other hand, the results obtained at HUNS were relatively noisy
 285 (low statistics) due to the shallow Bragg-dips as discussed in Fig. 6 (b). In addition, since
 286 the bottom side of Fig. 9 (a) corresponds to the outside region of the supermirror guide-
 287 tube, the statistical error becomes larger than on the upper side. However, the grain
 288 orientations evaluated at HUNS were consistent with those evaluated at J-PARC,
 289 although the sample alignments were slightly different as discussed above. In any case, it
 290 was confirmed that grain-orientation imaging using the Bragg-dip transmission method

291 is also feasible at a pulsed CANS using a decoupled moderator, although the Bragg-dip
292 analysis is more difficult than the Bragg-edge analysis due to low wavelength and angular
293 resolutions.

294

295



296

297 Fig. 9. Comparison of quantitative results of grain-orientation imaging, using an inverse
298 pole figure (IPF). Images were obtained at (a) HUNS and (b) J-PARC. The white dashed
299 lines of the HUNS result correspond to the separation positions between the sample pieces.
300 Fig. 9 (b) (the J-PARC result) is reproduced with permission of the International Union
301 of Crystallography from Ref. [6].

302

303 **3. Preliminary Monte-Carlo simulation study of a cold-neutron** 304 **moderator with decoupled pre-moderators and poisoned pre-** 305 **moderators**

306 In the previous section, we report that the strain imaging using the Bragg-edge method
307 and the grain-orientation imaging using the Bragg-dip method are feasible at a pulsed
308 CANS using a decoupled thermal-neutron moderator. However, although a supermirror
309 guide-tube was used, the neutron flux was still insufficient, suggesting the need for a cold-
310 neutron moderator. As such a moderator, one can use a multiple-stage moderation system,
311 like a coupled moderator consisting of a cold-neutron main-moderator combined with a
312 thermal-neutron pre-moderator. This work investigated two possibilities for an improved
313 system: a cold-neutron main-moderator with a thermal-neutron pre-moderator and a
314 decoupler, and a cold-neutron main-moderator with a poisoned pre-moderator. The cold-
315 neutron pulse characteristics of these new moderator systems were analyzed via a Monte-
316 Carlo simulation, and the results compared with conventional coupled, decoupled and
317 poisoned cold-neutron moderators.

318

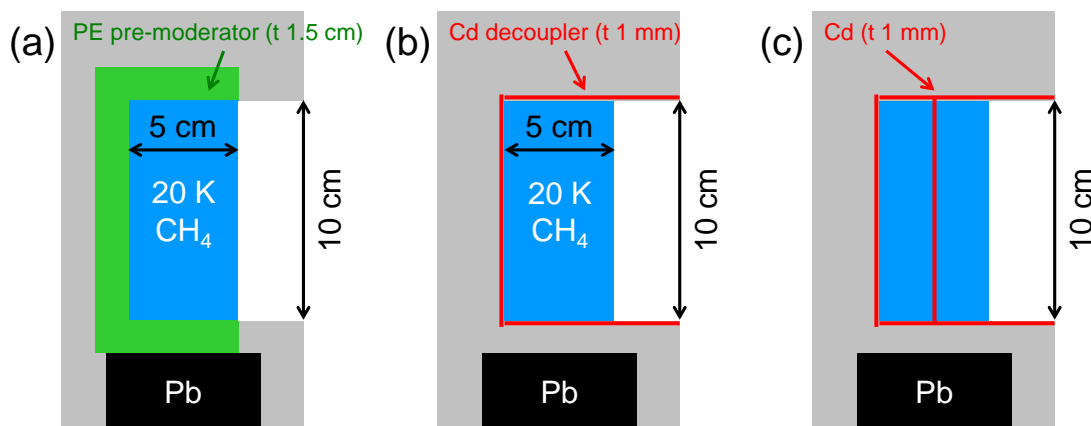
319 3.1. Calculation method, calculation geometry, and evaluation method

320 The Monte-Carlo neutron transport simulation code used in this calculation was the
321 Particle and Heavy Ion Transport Code System (PHITS) Version 2.820 [15]. We
322 compared the neutron pulse shapes (neutron emission time distributions) of cold neutrons
323 (5 meV) for five types of moderator.

324 The target material was lead ($7\text{ cm} \times 7\text{ cm} \times 7\text{ cm}$) as a photo-neutron source (black
325 materials in Figs. 10 and 11). The reflector material was graphite (gray materials in Figs.
326 10 and 11), and the reflector thickness was 40 cm, which can provide neutrons of saturated
327 intensity.

328 Fig. 10 shows the conventional moderator system designs for obtaining reference data.
329 The main-moderator for all types was 20 K methane of 5 cm thickness and 10 cm \times 10
330 cm area. The coupled moderator has a polyethylene pre-moderator of 1.5 cm thickness at
331 300 K. The decoupled moderator used in the simulation has a cadmium decoupler of 1
332 mm thickness instead of a pre-moderator. The decoupled-poisoned moderator contains a
333 cadmium plate of 1 mm thickness at the half thickness (2.5 cm) position in the moderator.
334 These moderator geometries were adopted for HUNS to maximize the total neutron flux,
335 and were not optimized in terms of both brightness for high L/D experiments and
336 wavelength resolution.

337



338

339 Fig. 10. Design of moderators used in simulation study. (a) A coupled cold-neutron
340 moderator; (b) a decoupled cold-neutron moderator; (c) a decoupled-poisoned cold-
341 neutron moderator. The dimensions of the main-moderator (20 K methane) are 5 cm in
342 thickness, 10 cm in height, and 10 cm in width.

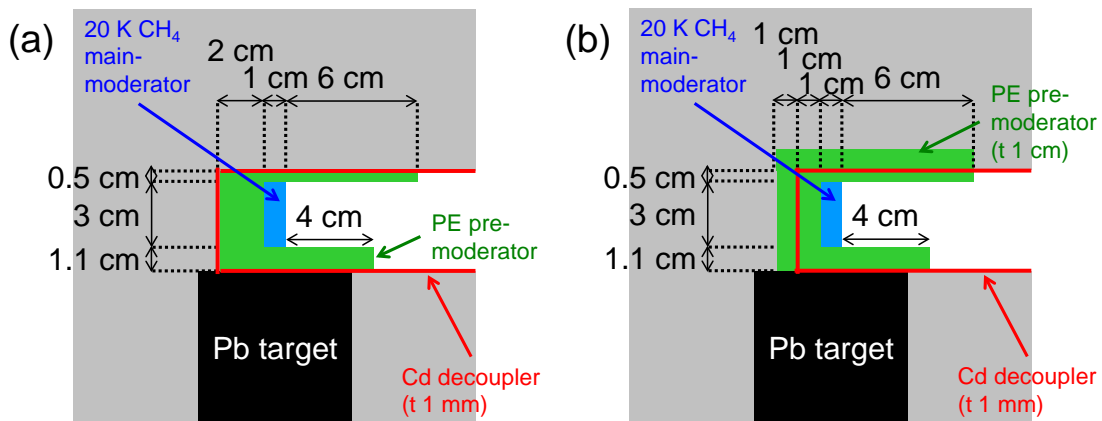
343

344 Fig. 11 (a) shows a new type of moderator; a cold-neutron moderator with decoupled
345 pre-moderators. This geometry corresponds to a coupled moderator with a decoupler. This

346 design has already been optimized by iterative Monte-Carlo simulation studies, which
 347 highlight the importance of a main-moderator that is (i) thin (1 cm thickness) for narrow
 348 neutron pulse, and (ii) low profile (3 cm in height) for effective use of the high brightness
 349 region near the target. The simulations also suggested the need for pre-moderators with
 350 large solid-angle coverage (7 cm (floor) and 9 cm (roof)) for fast neutrons emitted from
 351 the target. Furthermore, Fig. 11 (b) shows a second new type of moderator: a cold-neutron
 352 moderator with poisoned pre-moderators. This geometry corresponds to a cold-neutron
 353 moderator with a decoupled pre-moderator and additional pre-moderators, or a moderator
 354 with poisoned pre-moderators. The design presented in this figure was also optimized by
 355 iterative Monte-Carlo simulation studies. The important points are the same as those for
 356 the decoupled pre-moderator system. As an additional feature, the backside pre-moderator
 357 thickness becomes thinner owing to the poison, from 2 cm to 1 cm. The main-moderator
 358 consists of 20 K methane (1 cm \times 3 cm \times 10 cm), the pre-moderator is 300 K polyethylene,
 359 and the decoupler is cadmium.

360 The neutron emission time distributions (pulse shapes) for these five types of
 361 moderator system, were evaluated by Monte-Carlo simulation. The evaluated neutron
 362 energy was 5 meV (0.4 nm wavelength). The evaluated beam angular divergence range
 363 was within $\pm 30^\circ$ around the neutron beam-line axis. The evaluated moderator surface
 364 region was defined to be a 1 cm \times 1 cm area of highest neutron brightness because high
 365 L/D experiments (pinhole collimator use) were considered. The data were normalized to
 366 one fast neutron generated from the target.

367



368

369 Fig. 11. Moderator geometries used in the simulation. (a) A cold-neutron moderator with
 370 decoupled pre-moderators; (b) a cold-neutron moderator with poisoned pre-moderators.
 371 The dimensions of the main-moderator (20 K methane) are 1 cm in thickness, 3 cm in
 372 height, and 10 cm in width.

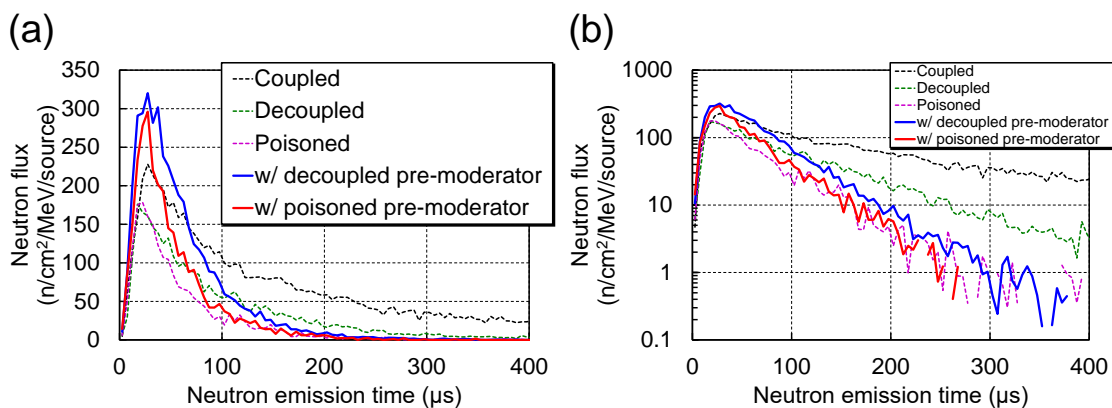
373

374 **3.2. Results and discussion**

375 Fig. 12 shows plots of cold neutron fluxes using each of the moderator systems; Fig.
 376 12 (a) is plotted using a linear scale to evaluate the peak intensity and the pulse width,
 377 and Fig. 12 (b) employs a semi-log scale to evaluate the pulse decay. Table 1 presents a
 378 comparison of the moderator systems in terms of the peak intensity, pulse width (FWHM),
 379 and pulse decay (1/10 pulse width). The two types of moderator proposed in this work
 380 have the highest peak intensity (higher than a conventional coupled moderator). On the
 381 other hand, these new moderator systems have narrow pulse widths, about the same as
 382 those achieved by the decoupled moderator (60 μs) and the poisoned moderator (40 μs)
 383 (see Table 1). In addition, the decay time of these new moderator systems match that of
 384 the poisoned moderator (about 120 μs , see Fig. 12 (b) and Table 1). The reason that the
 385 poisoned pre-moderator system has a narrower pulse width than the decoupled pre-
 386 moderator system is the thickness of the inner pre-moderator. In other words, as
 387 mentioned above, the backside pre-moderator can be made thinner (from 2 cm to 1 cm)
 388 owing to the presence of the poison layer. The reason that the poisoned pre-moderator
 389 system has the same peak intensity as the decoupled pre-moderator system is the existence
 390 of the outer pre-moderators.

391 This study suggests the possibility of new moderator systems which simultaneously
 392 use both a pre-moderator and a decoupler (or poison), and it is feasible that both higher
 393 peak intensity and sharper neutron pulses can be simultaneously achieved in terms of high
 394 brightness (high L/D experiment). This can help to improve the “shallow dip depth”
 395 problem in a Bragg-dip neutron transmission imaging experiment at a pulsed CANS.

396



397
 398 Fig. 12. Cold neutron emission time distributions for each moderator system, expressed
 399 on (a) a linear scale and (b) a semi-log scale.

400

401 Table 1. Comparison of peak intensity, pulse width (FWHM), and decay time (1/10 pulse

402 width) of cold-neutron pulses for each moderator system.

Moderator type	Peak intensity (n/cm ² /MeV/source)	Pulse width (FWHM) (μ s)	1/10 pulse width (μ s)
Coupled moderator	225	80	400
Decoupled moderator	175	60	200
Poisoned moderator	175	40	125
Decoupled pre-moderator system	300	55	130
Poisoned pre-moderator system	300	40	110

403

404 **4. Conclusion**

405 By using a supermirror guide-tube coupled to a decoupled thermal-neutron moderator
406 (polyethylene at ambient temperature), we achieved strain imaging using the Bragg-edge
407 transmission method and grain-orientation imaging using the Bragg-dip transmission
408 method, under the condition of 0.5% wavelength resolution at a compact-accelerator
409 driven pulsed-neutron source. Although there is room for improvement in neutron flux
410 and neutron beam angular divergence (in particular, for the Bragg-dip transmission
411 method), measured strain values and grain orientations agreed well with the results of the
412 J-PARC experiments.

413 Monte-Carlo simulations were performed to evaluate the performance of a thin and
414 low-height cold-neutron moderator (20 K methane) with the new components, a
415 decoupled pre-moderator and a poisoned pre-moderator with large solid-angle coverage
416 for fast neutrons. The results suggest that these components offer higher peak intensity
417 than a coupled moderator (about 1.3 times higher), the same pulse width as
418 decoupled/poisoned moderators (about 60 or 40 μ s), and the same decay time as a
419 poisoned moderator (about 120 μ s). Note that these values were attained only over a
420 certain region (1 cm \times 1 cm) of highest neutron brightness. In other words, these
421 moderator modifications are suitable for high L/D experiments with low beam angular
422 divergence using a pinhole collimator. Further detailed investigations are necessary to
423 more fully characterize these new types of moderator systems.

424

425 **Acknowledgements**

426 The authors are thankful to Prof. Yoshiaki Kiyonagi of Nagoya University for
427 invaluable discussions, and Mr. Koh-ichi Sato of Hokkaido University for accelerator
428 operations and experimental assistances. This work was partially supported by JSPS

429 KAKENHI Grant Number 16K20876.

430

431 **References**

- 432 [1] H. Sato, Y. Shiota, T. Kamiyama, M. Ohnuma, M. Furusaka and Y. Kiyonagi, Phys.
433 Procedia **60** (2014) 254-263.
- 434 [2] H. Sato, T. Kamiyama and Y. Kiyonagi, Mater. Trans. **52** (2011) 1294-1302.
- 435 [3] H. Sato, T. Shinohara, R. Kiyonagi, K. Aizawa, M. Ooi, M. Harada, K. Oikawa, F.
436 Maekawa, K. Iwase, T. Kamiyama and Y. Kiyonagi, Phys. Procedia **43** (2013) 186-
437 195.
- 438 [4] H. Sato, T. Sato, Y. Shiota, T. Kamiyama, A. S. Tremsin, M. Ohnuma and Y. Kiyonagi,
439 Mater. Trans. **56** (2015) 1147-1152.
- 440 [5] H. Sato, Y. Shiota, T. Shinohara, T. Kamiyama, M. Ohnuma, M. Furusaka and Y.
441 Kiyonagi, Phys. Procedia **69** (2015) 349-357.
- 442 [6] H. Sato, Y. Shiota, S. Morooka, Y. Todaka, N. Adachi, S. Sadamatsu, K. Oikawa, M.
443 Harada, S. Y. Zhang, Y. H. Su, T. Kamiyama, M. Ohnuma, M. Furusaka, T. Shinohara
444 and Y. Kiyonagi, J. Appl. Crystallogr. **50** (2017) 1601-1610.
- 445 [7] M. Furusaka, H. Sato, T. Kamiyama, M. Ohnuma and Y. Kiyonagi, Phys. Procedia
446 **60** (2014) 167-174.
- 447 [8] H. Sato, K. Mochiki, K. Tanaka, K. Ishizuka, H. Ishikawa, T. Kamiyama and Y.
448 Kiyonagi, *A new high-speed camera type detector for time-of-flight neutron imaging*
449 *and its application to crystalline phase analysis at a coupled-moderator based pulsed*
450 *neutron source driven by a compact accelerator*, Nucl. Instrum. Methods A, in
451 preparation.
- 452 [9] T. Shinohara, T. Kai, K. Oikawa, M. Segawa, M. Harada, T. Nakatani, M. Ooi, K.
453 Aizawa, H. Sato, T. Kamiyama, H. Yokota, T. Sera, K. Mochiki and Y. Kiyonagi, J.
454 Phys. Conf. Ser. **746** (2016) 012007.
- 455 [10] Y. Kiyonagi, N. Watanabe and H. Iwasa, Nucl. Instrum. Methods A **312** (1992) 561-
456 570.
- 457 [11] K. Oikawa, F. Maekawa, M. Harada, T. Kai, S. Meigo, Y. Kasugai, M. Ooi, K. Sakai,
458 M. Teshigawara, S. Hasegawa, M. Futakawa, Y. Ikeda and N. Watanabe, Nucl.
459 Instrum. Methods A **589** (2008) 310-317.
- 460 [12] S. Uno, T. Uchida, M. Sekimoto, T. Murakami, K. Miyama, M. Shoji, E. Nakano, T.
461 Koike, K. Morita, H. Satoh, T. Kamiyama and Y. Kiyonagi, Phys. Procedia **26** (2012)
462 142-152.
- 463 [13] S. Harjo, T. Ito, K. Aizawa, H. Arima, J. Abe, A. Moriai, T. Iwahashi and T.
464 Kamiyama, Mater. Sci. Forum **681** (2011) 443-448.

- 465 [14]A. S. Tremsin, J. B. McPhate, A. Steuer, W. Kockelmann, A. M. Paradowska, J. F.
466 Kelleher, J. V. Vallerga, O. H. W. Siegmund and W. B. Feller, *Strain* **48** (2012) 296-
467 305.
- 468 [15]T. Sato, K. Niita, N. Matsuda, S. Hashimoto, Y. Iwamoto, S. Noda, T. Ogawa, H.
469 Iwase, H. Nakashima, T. Fukahori, K. Okumura, T. Kai, S. Chiba, T. Furuta and L.
470 Sihver, *J. Nucl. Sci. Tech.* **50** (2013) 913-923.